



A dual-balance strategy via phosphate modification on $\text{MnO}_2\text{-CeO}_2$ for NO_x and chlorobenzene synergistic catalytic control

Xiao Zhu^a, Xing Yuan^a, Zijian Song^b, Yue Peng^{a,*}, Junhua Li^a

^a State Key Joint Laboratory of Environment Simulation and Pollution Control, School of Environment, Tsinghua University, Beijing 100084, China

^b China National Institute of Standardization, Beijing 100191, China



ARTICLE INFO

Keywords:

SCR
Chlorobenzene
Reducibility
Phosphate
Acidity

ABSTRACT

Traditional $\text{MnO}_2\text{-CeO}_2$ (MnCe) exhibits efficient synergistic-control performance for selective catalytic reduction of NO_x and chlorobenzene (CB) oxidation. However, the issues of N_2O formation and chlorine-deposition remain challenges. Herein, a phosphate-modified MnCe exhibits both higher NO_x and CB conversions than MnCe: N_2O formation decreases by 23%, while HCl selectively increases by 10% at 300 °C. Phosphate widens the band gap of Mn 3d of MnCe and recovers the bond length of Ce-O back to that of ceria, restricting the electrons transfer from surface cations to chlorine ions by the orbital polarization effect. Meanwhile, phosphate also provides more Brønsted and weakly Lewis acid sites, favoring CB nucleophilic substitutions rather than polychlorinated species accumulation. Both the chlorine adsorption energy and HCl formation barrier decrease after phosphate modification. This work provides a novel modulation strategy of dual-balance (reducibility vs. total acidity; Lewis vs. Brønsted) on the design of multi-pollutant control catalysts.

1. Introduction

Environmental catalysts are typically designed to efficiently control a specific pollutant, ensuring high catalytic activity, selectivity, and stability towards particular harmless products. Selective catalytic reduction (SCR) using NH_3 is one of the substantial technologies to remove NO_x from stationary burning sources and diesel engines [1–4]. However, actual situations often involve complex scenarios with multi-pollutants coexisting at distinct concentrations. In most cases, these pollutants exhibit disparate features such as reaction atmosphere, acid-base and redox properties of reactants. NO_x and chlorinated volatile organic compounds (CVOCs) are simultaneously emitted from steel sintering, cement kiln and waste incinerator, with CVOCs concentrations ranging from only 0.1–10% of NO_x . In addition, NO_x cleaning is a reduction process using NH_3 , whereas, CVOCs cleaning is an oxidation process using O_2 [5–8]. Therefore, achieving efficient control of NO_x and CVOCs simultaneously (multi-pollutant control, MPC) in a ready-made catalyst system is quite difficult.

One plausible method is constructing new active dopants with good CVOCs oxidation ability on traditional SCR catalysts. The Pd-doped $\text{V}_2\text{O}_5\text{/TiO}_2$ catalyst exhibits enhanced oxidation activity towards chlorobenzene (CB) under the premise of excellent NO_x conversion, but

shows low N_2 selectivity due to the N_2O formation, or even Cl_2 formation at high temperatures via Deacon reaction [9,10]. $\text{MnO}_2\text{-CeO}_2$ catalyst exhibits excellent performance for NO_x and CB synergistic control [11,12]. High reducibility of Mn promotes the NO oxidation, thereby facilitating CB oxidation through NO_2 . Furthermore, N_2O formation at high temperatures is also alleviated by suppressing NH_3 unselective oxidation. However, $\text{MnO}_2\text{-CeO}_2$ still faces certain limitations, including narrow temperature window, N_2O formation, and chlorine deposition, which are caused by over-strong reducibility and Lewis acid sites.

Modulating SCR catalyst involves achieving a balance between the reducibility and total acidity of active sites [13,14]. Abundant acid sites enhance SCR activity through facilitating NH_3 adsorption, whereas, reducibility is closely associated with N_2 selectivity. Meanwhile, balancing the number and strength of the Lewis and Brønsted acid sites is essential for CB oxidation [15–17]. Brønsted acid sites promote the migration of chloride ions via nucleophilic substitutions, thereby facilitating the formation of desired phenol and HCl. While Lewis acid sites participate in the cleavage of C-Cl bonds, excessive strength can lead to the accumulation of chloride ions (di- or poly- chlorides) on the surface via an electrophilic chlorination reaction. Phosphorus has been considered as an inhibitor for vanadia-based SCR catalysts [18,19],

* Correspondence to: State Key Joint Laboratory of Environment Simulation and Pollution Control, School of Environment, Tsinghua University, Beijing.
E-mail address: pengyue83@tsinghua.edu.cn (Y. Peng).

however, it is also reported to enhance the SCR activity of CeO_2 by increasing the number and strength of Brønsted acid sites [20]. In addition, phosphate has also been demonstrated to act as a promoter for CB oxidation, because it could improve CB oxidation with good HCl selectivity and CO_2 yield via a hydrolytic destruction route, and compromises the over-strong redox property of catalysts due to partial coverage of active sites [13,21–23]. Therefore, it is reasonable to modulate the reactivity of surface-active sites on $\text{MnO}_2\text{-CeO}_2$ catalysts, and the modulation also requires a molecular understanding of the mechanism.

In this work, a phosphate-modified $\text{MnO}_2\text{-CeO}_2$ was prepared via a wet-impregnation method. The reducibility, surface acidity and chlorine deposition were studied. The electronic structure, charge population and reaction pathway were calculated according to density functional theory (DFT). The dual-balance strategy by phosphate modification was discussed and proposed.

2. Experimental and calculation methods

2.1. Catalyst preparation

The $\text{MnO}_2\text{-CeO}_2$ catalyst was synthesized via a coprecipitation method and the molar ratio of Mn:Ce is 4:6 (MnCe). The phosphate-modified $\text{MnO}_2\text{-CeO}_2$ catalyst was prepared via a wet impregnation method, and the loading of phosphate is 1 wt% (P/MnCe). We also prepared a series of phosphate-modified catalysts with different phosphate loading amounts. More synthesis details are provided in the Supporting Information (SI).

2.2. Catalyst characterization

The details of H_2 -temperature programmed reduction ($\text{H}_2\text{-TPR}$), O_2 -temperature programmed desorption ($\text{O}_2\text{-TPD}$), X-ray diffraction (XRD), electron paramagnetic resonance (EPR), N_2 adsorption-desorption, X-ray photoelectron spectroscopy (XPS), NH_3 -temperature programmed desorption ($\text{NH}_3\text{-TPD}$), high resolution transmission electron microscope (HRTEM) with energy dispersive spectrometry (EDS) mapping, in-situ diffuse reflectance infrared Fourier transform spectroscopy (in-situ DRIFTS) are provided in the SI. The deposited species on the surface of used catalysts (uMnCe and uP/MnCe) were analyzed via a coupling technique combined of thermogravimetric, infrared spectrometer, and mass spectrometry (TG-IR-MS).

2.3. Performance measurement

The MPC performance of the catalysts were evaluated in a fixed-bed system. The total flow rate of flue gas was 100 mL min^{-1} , consisting of 500 ppm NO, 500 ppm NH_3 , 100 ppm CB, 10% O_2 and 3% H_2O , and balanced N_2 . 100 mg of sample was used in each test under the space velocity of $60,000 \text{ cm}^3 \text{ g}^{-1} \text{ h}^{-1}$. The inlet and outlet gas concentrations were measured by GASMET DX-4000. The calculation equations of NO_x and CB conversion and the selectivity are provided in the SI.

2.4. DFT+U calculation

The DFT calculations are employed on Vienna Ab-initio Simulation Package (VASP 5.4.4) [24]. The values of U_{eff} for Mn and Ce were both set as 5.0 eV using the DFT+U method. The models were constructed by cutting the most stable CeO_2 surface (1 1 1) (CeO_2), and replaced a surface Ce atom by Mn (MnCeO_2) and a PO_x cluster-doped (P/MnCeO_2) models [25–27]. The corresponding models with surface oxygen vacancy were denoted as MnCeO_v and P/MnCeO_v , respectively. More detailed on transition state (TS) search, adsorption energy (E_{ads}), oxygen vacancy formation energy (E_{ov}), and energy barrier (E_b) are provided in the SI.

3. Results and discussion

3.1. Catalytic performance

Fig. 1a illustrates the MPC performance of the MnCe and P/MnCe catalysts. The P/MnCe exhibits higher NO_x and CB conversions than the MnCe above 150 °C. Additionally, N_2O production is partially suppressed above 200 °C, and outlet concentration decrease by approximately 23% at 325 °C (Fig. S2). The MPC performance of the other catalysts with higher phosphate loadings is also performed (Fig. S2), and they show higher SCR activities and lower N_2O formations than the MnCe, suggesting that phosphate might suppress the over-oxidation of NH_3 , thereby improving NO_x conversion and N_2 selectivity [28]. The selectivities of desired products, including HCl and CO_2 , for both MnCe and P/MnCe catalysts are depicted in Fig. 1b. The P/MnCe also possesses more CO_2 and HCl than that the MnCe below 325 °C. Both CO_2 selectivity and HCl selectivity of P/MnCe catalyst at 325 °C reach 90%. Moreover, large amount of phosphate considerably decreases CB conversion (Fig. S3) and CO_2 selectivity below 300 °C, which could be attributed to the loss of reducibility. Table S1 provides a summary of the catalytic performance of P/MnCe catalyst and other catalysts reported in the literature for NO_x and CB synergistic control. CB conversion of P/MnCe catalyst at 300 °C reached 87%, which is outstanding in comparison with that of the reported catalysts. Considering that Deacon reaction (Cl_2 formation) usually occurs above 350 °C on noble-metal catalysts, the remnant chlorinates and HCs could be attributed to the decomposition species on catalysts. In other words, carbon and chlorine accumulation are significantly alleviated by the phosphate introduction.

Based on our previous results, the total chlorine species could be divided into three categories in the MPC reactions: gaseous HCl/Cl_2 , chlorinated-surface cations (M-Cl), and surface-deposited chlorinated-hydrocarbons (HCs-Cl) [29]. To further understand the influence of phosphate on the migration and transformation of chlorine species, the consumed CB and outlet HCl on the MnCe and P/MnCe at 300 °C are shown in Fig. 1c and d, respectively. The consumed CB of MnCe decreases gradually and reaches approximately 50 ppm in 6 h, whereas, the chlorine deposition extent of P/MnCe is obviously milder, with 70 ppm of consumed CB in 6 h. The formed HCl on the P/MnCe is also higher by nearly 10–15 ppm than that on the MnCe. According to the equilibrium of chlorine, the total amount of Cl-containing species (M-Cl and HCs-Cl) should be equal to the difference between the consumed CB and outlet HCl. The calculated Cl-containing species of the uMnCe and uP/MnCe are 0.67 and 0.61 umol g^{-1} , respectively. The results illustrate that phosphate alleviates the chlorine deposition on the MnCe. Meanwhile, gaseous HCl releases as soon as the chlorine anchoring and release reaches an equilibrium. The initial release time on the P/MnCe is nearly 24 min earlier than that on the MnCe, validating that chlorine is more difficult to deposit on the P/MnCe. The stability of MnCe and P/MnCe in the MPC reactions at 275 °C is also performed (Fig. S4). The P/MnCe exhibits higher consumed CB and formed HCl than the MnCe, but lower stability compared with that at 300 °C.

In brief, phosphate modification enhances the MPC performance of the MnCe catalyst. In addition to the increased NO_x and CB conversions above 150 °C, the selectivities of N_2 , CO_2 , and HCl can be also improved. The side reactions of NH_3 unselective oxidation and surface chlorine-deposition are also suppressed.

3.2. Structure and redox properties

The XRD patterns (Fig. 2a) and BET surface areas (Table 1) of the MnCe and P/MnCe are similar, and no other peaks related to phosphate are observed. [28,30] The HRTEM images (Fig. S5) indicated that the phosphate modification did not significantly alter the crystal morphology of the P/MnCe catalyst. Additionally, EDS mapping images of P/MnCe revealed a homogeneous distribution of phosphate on the catalyst surface. The $\text{H}_2\text{-TPR}$ profiles of the catalysts (Fig. 2b) can be

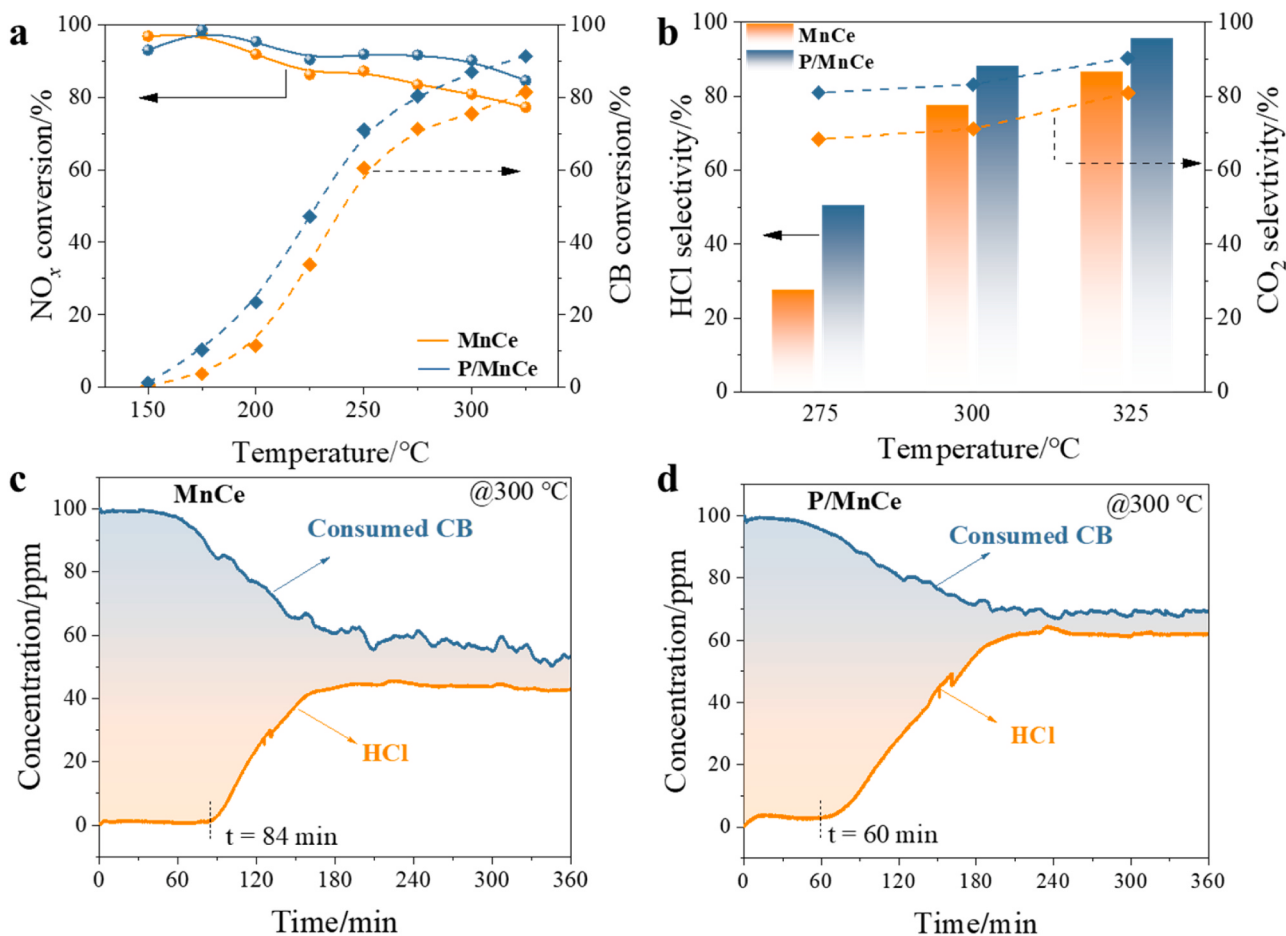


Fig. 1. Catalytic performance in the simultaneous removal of NO_x and CB: (a) the NO_x and CB conversions, and (b) the HCl and CO_2 selectivity of MnCe and P/MnCe catalysts. Consumed CB and outlet HCl concentrations of (c) MnCe, and (d) P/MnCe catalysts during the reactions at 300 $^{\circ}\text{C}$. Reaction conditions: $\text{NH}_3 = 500 \text{ ppm}$, $\text{NO} = 500 \text{ ppm}$, $\text{CB} = 100 \text{ ppm}$, $\text{O}_2 = 10\%$, $\text{H}_2\text{O} = 3\%$, N_2 as the balance gas, and GHSV = 60,000 $\text{mL g}^{-1} \text{ h}^{-1}$.

divided into low- and high-temperature regions. Low-temperature region ($< 550 \text{ }^{\circ}\text{C}$) is mainly attributed to the reduction process of MnO_x . The peaks of MnCe at 240 $^{\circ}\text{C}$ and 367 $^{\circ}\text{C}$ can be attributed to the reduction of Mn^{4+} to Mn^{3+} and Mn^{3+} to Mn^{2+} , respectively [31]. However, the corresponding peaks of P/MnCe slightly shift to higher temperatures, resulting in the inhibition of Mn reducibility. EPR spectra are employed to quantify the amounts of total oxygen vacancies of the catalysts (Fig. 2c and Table 1). The P/MnCe is more accessible for the formation of oxygen vacancies than the MnCe at $g = 2.003$. To further study the relationship between surface-active oxygen and surface oxygen vacancies, O 1 s (Fig. 2d), Mn 3 s (Fig. 2e) and Ce 3d (Fig. 2f) XPS spectra of the catalysts are performed. The O 1 s spectra could be deconvoluted into two peaks. The peaks at 529.7 and 531.2 eV can be assigned to the lattice oxygen (O_l) and oxygen species chemisorbed by surface oxygen vacancies (O_{II}), respectively [20]. The O_{II} proportion of P/MnCe is higher than that of MnCe (Table 1), indicating a higher amount of chemisorbed oxygen species. O_2 -TPD profiles are employed to evaluate oxygen storage capacity (Fig. S11). The desorption of oxygen between 50 and 300 $^{\circ}\text{C}$ is attributed to surface-adsorbed oxygen species, and the corresponding integrated amounts of oxygen desorption are listed in Table 1. Consistent with the O_{II} proportions, P/MnCe exhibits a higher amount of adsorbed oxygen after excluding the influence of S_{BET} . In addition, a new peak around 533.0 eV appears, which is attributed to the adsorbed molecular H_2O [32]. The average oxidation state (AOS) of Mn can be calculated based on the doublet splitting energy of Mn 3 s peaks [23], the Mn AOS of P/MnCe is lower than that of MnCe, indicating that partial reductions of Mn cations on the surface occur by the phosphate introduction. Mn 2p results also

verify the observed trend (Fig. S7b and Table 1). The Mn 2p_{3/2} spectra exhibit two peaks at approximately 642.3–642.7 eV and 640.7–640.9 eV, corresponding to low valence manganese (Mn^{4+}) and high valence manganese ($\text{Mn}^{2+}/\text{Mn}^{3+}$), respectively [26,33]. Ce 3d peaks can be deconvoluted into ten peaks, in which v' , u' , u^0 , and v^0 are assigned to Ce^{3+} , while the others are assigned to Ce^{4+} [34]. The Ce^{3+} proportion of P/MnCe is higher than that of MnCe. The results suggest that there might be an interaction among P, Mn and Ce via bridging O.

Since phosphate decreases the valence states of both surface Mn and Ce. It is reasonable to assume that the influence of phosphate on surface Mn-O-Ce species is by achieving the changes in the bond length and Bader charge. We calculate the bond length of surface Ce-O in three DFT models, CeO_2 , MnCeO_2 and P/MnCeO₂ (Fig. 2g). The bond length of Ce-O recovers from 2.18 Å in MnCeO_2 to 2.42 Å in P/MnCeO₂, which is similar as that in CeO_2 (2.37 Å). In addition, phosphate leads to a decrease in the charge density on the bridging O of Mn-O-Ce species (from 1.06 to 0.59) (Fig. S8). Moreover, we calculate the formation energy of singlet oxygen vacancy (E_v) on the Mn-O-Ce species (Fig. 2h). The E_v of MnCeO_2 is higher than that of P/MnCeO₂, which further confirms the XPS and O_2 -TPD results. We have also calculated the H_2O adsorption on the oxygen vacancies (Fig. S12), and the results show that phosphate promotes the H_2O adsorption from -0.88 eV to -1.21 eV . The Bader charges of both Mn and Ce decrease by the phosphate introduction (Fig. S9), suggesting that the electrons transfer from bridged O to surface cations by the partial reduction. The enrichment of electrons at Mn and Ce cations might show a certain influence on the migration and activation of NH_3 and Cl ions on the catalyst surface.

As known, most of dopants (Cu, Fe, Co etc.) on MnO_2 -CeO₂ surface

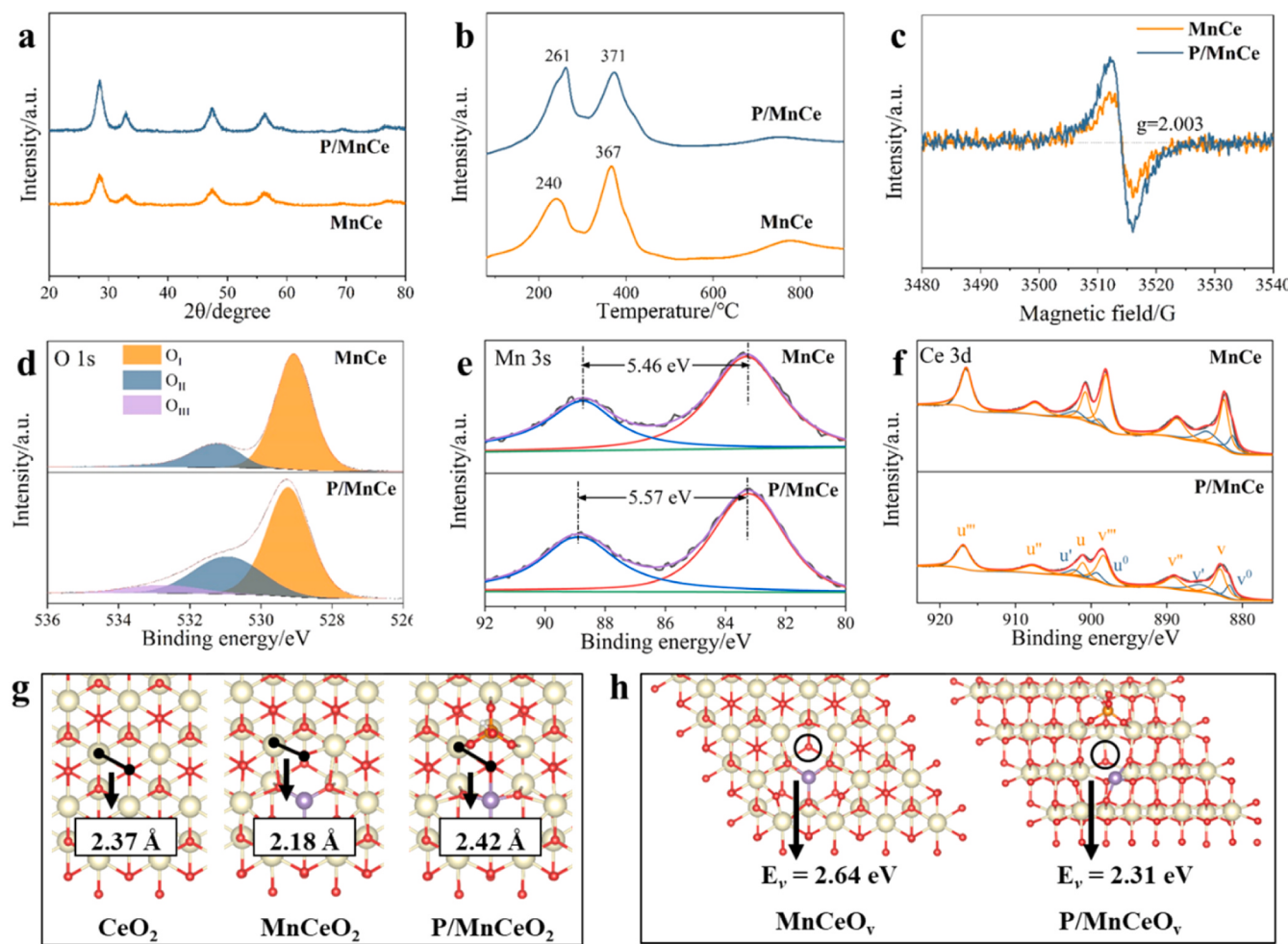


Fig. 2. (a) XRD, (b) H₂-TPR, and (c) EPR spectra of MnCe and P/MnCe catalysts. XPS spectra of (d) O 1 s, (e) Mn 3 s, and (f) Ce 3d of MnCe and P/MnCe catalysts. (g) The length of surface Ce-O bond near the Mn cations of CeO₂, MnCeO₂ and P/MnCeO₂ models, and (h) oxygen vacancy formation energy (E_v) of MnCeO_v and P/MnCeO_v models. (Mn is purple, Ce is yellow, P is orange, H is white, and O is red.).

Table 1
Surface chemical property of the catalysts.

	S_{BET} (m ² /g)	AOS of Mn ^a	Mn_{sur}^{4+} (%)	Ce_{sur}^{3+} (%)	O_{II} (%)	$O_{\text{des},50-300}$ (μmol/m ²)	$O_v (10^{14} \text{ spins/g})^{b,c}$
MnCe	89.5	2.84	51.2	20.9	22.5	2.6	4.3
P/MnCe	87.4	2.71	44.5	25.9	31.9	3.3	7.4

^a AOS = $(8.001 - \Delta E) / 0.896$ (ΔE represents the doublet splitting energy of Mn 3 s)

^b Oxygen desorption amounts at 50 – 300 °C normalized by the S_{BET}

^c Calculated by the EPR spectra.

shows an improvement in both the reducibility of Mn and the oxygen vacancies because of their excellent electronic acceptor characteristic and electronegativity [35–37]. Unlike their intrinsic properties, phosphate exhibits a slightly inhibition effect on the reducibility of Mn and Ce. It even changes the bond length of Ce-O back to a similar length as pure CeO₂ (111), leading to the mitigation of the over-strong reducibility of P/MnCeO₂ catalyst. However, the phosphate modification increases the number of oxygen vacancies increases, thereby facilitating the adsorption of O₂ and H₂O. The surface characteristics of the used catalysts are also analyzed (Fig. S10). Apparent chlorine deposition also decreases.

In brief, phosphate widens the band gap of Mn 3d of MnCe and recovers the bond length of Ce-O back to that of CeO₂, mitigating the over-strong reducibility of Mn. The energies of NH₃ adsorption at Lewis acid sites and oxygen vacancy formations decreased.

3.3. Surface acidity and influence on NH₃ and CB

In situ DRIFTS spectra of pyridine adsorptions on the catalysts are employed to semi-quantitative the acidic sites (Fig. 3a). The bands around 1450 and 1605 cm⁻¹ can be attributed to the adsorbed pyridine on the Lewis acid sites, while the peaks at 1540 and 1640 cm⁻¹ can be assigned to the Brønsted acid sites. The peak at 1490 cm⁻¹ is attributed to the total acid sites [38,39]. Here we use the peaks at 1450, 1540 and 1490 cm⁻¹ to quantify the amount of Lewis, Brønsted and total acid sites on the catalysts, respectively. The P/MnCe exhibits similar Lewis acid sites in quantity, but larger Brønsted acid sites than the MnCe at 100 °C, suggesting that phosphate improves predominantly Brønsted acid sites of MnCe. With increasing the temperature up to 300 °C, though the number of both acid sites decreases, however, the amount of Brønsted acid sites (Fig. 3b) on the P/MnCe is still greater than that on the MnCe.

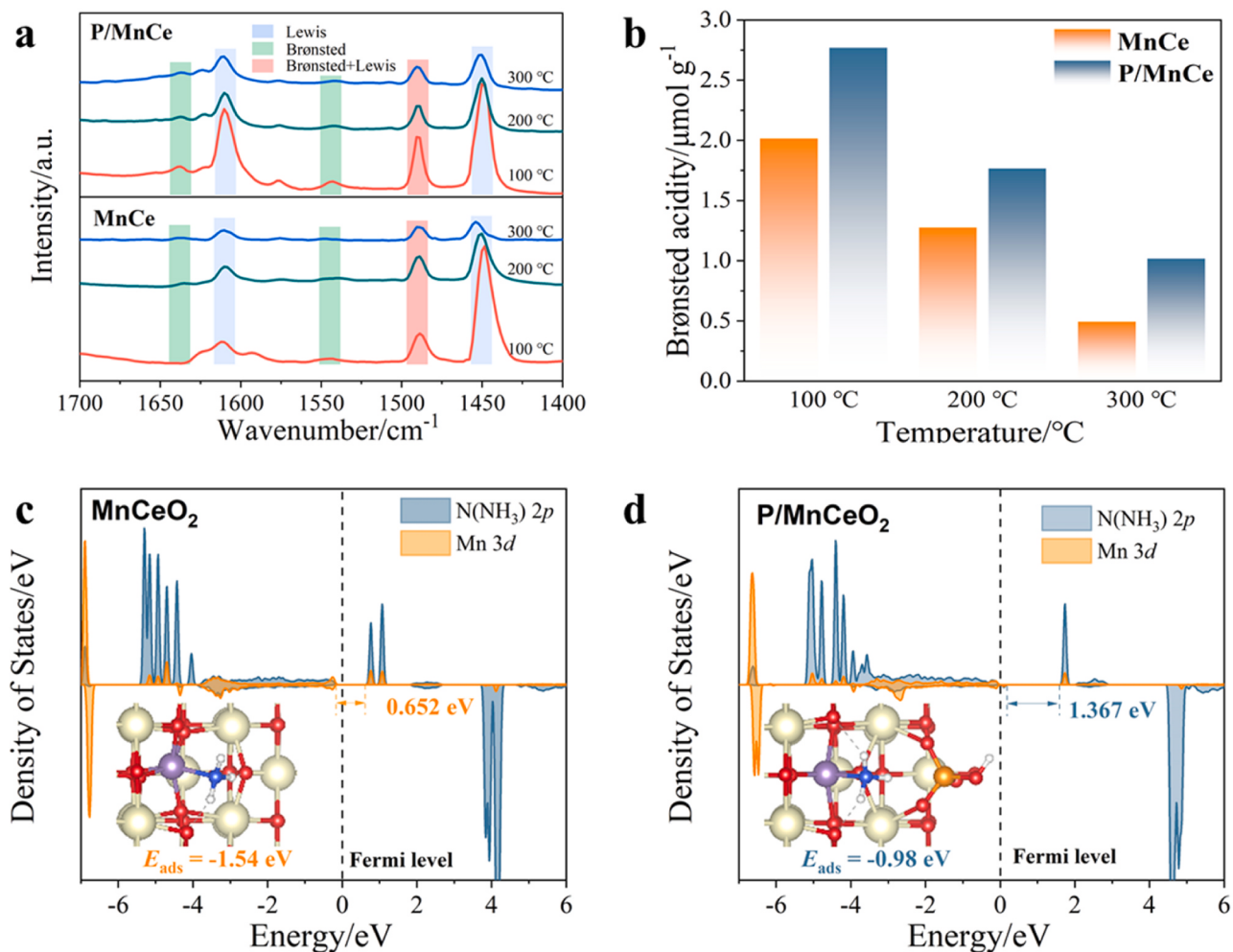


Fig. 3. In situ DRIFTS of (a) pyridine adsorption in 100–300 °C, (b) Semiquantitative amount of Brønsted acid sites of MnCe and P/MnCe catalysts. Density of states and adsorption configurations of NH₃ at Lewis acid sites on the (c) MnCeO₂ and (d) P/MnCeO₂ models.

Furthermore, the thermal stability of Lewis acid sites (mainly Mn cations) on the P/MnCe is also weaker than that on the MnCe. It is easy to understand that phosphate itself can serve as Brønsted acid sites on the catalyst surface, which is crucial for the C-Cl cleavage of CB. On the other hand, the interactions between phosphate and Mn weaken the stability of Lewis acid sites, beneficial for the inhibition of electrophilic chlorination of CB.

The density of state (DOS) of Mn 3d and N 2p orbitals and the NH₃ adsorption energy (E_{ads}) on the MnCeO₂ and P/MnCeO₂ models are calculated (Fig. 3c-d). Phosphate-doped surface presents a wider band gap of Mn 3d (1.367 eV): the bottom of conduction band shifts to higher energy, inhibiting the electron transfer from N 2p orbitals to the unoccupied Mn 3d orbitals. The absolute value of NH₃ E_{ads} on the P/MnCeO₂ is higher than that on the MnCeO₂, suggesting that the thermal stability of NH₃ adsorptions on the Lewis acid sites decreases by the phosphate introduction. Combined with the results of Fig. 3a, we propose that phosphate-induced Lewis acid sites are more in quantity but poor in stability. These acid sites could still provide enough NH₃ adsorption for SCR reaction at relatively low temperatures, but less formation of polychlorinated species via electrophilic chlorination reactions above 300 °C.

To further study the influence of phosphate on NH₃ and CB activation, in situ DRIFTS of NH₃ reaction with surface-active oxygen (Fig. 4a-b) and CB reaction with gaseous oxygen (Fig. 4c-d) are performed respectively. After NH₃ adsorption at 50 °C, four peaks at 1598, 1431, 1294 and 1156 cm⁻¹ can be attributed to coordinated NH₃ adsorption

on Lewis acid sites, whereas the peak at 1431 cm⁻¹ can be attributed to NH₄⁺ adsorption on Brønsted acid sites. As for the P/MnCe, the peak intensity of NH₄⁺ bonded with Brønsted acid sites is significantly higher, especially at high temperatures, than that on the MnCe. The peak at 1294 cm⁻¹ of both the catalysts in 50–200 °C can be assigned to the bidentate nitrate, which is due to the oxidation of NH₃ with surface-active oxygen [37], suggesting that the NH₃ oxidation activity at low temperature is not significantly influenced by the phosphate introduction, ensuring the formation of NH_x radicals to fulfill the SCR cycles.

As for the in-situ DRIFTS spectra of CB oxidation at 300 °C, several bands located at 1214, 1304, 1522, 1556, and 1614 cm⁻¹ are observed at the initial stages of CB oxidation on the MnCe. The band at 1214 cm⁻¹ can be assigned to the phenol species from the replacement of Cl or H by hydroxyls. [40]. In addition, the key intermediates of maleate or chloromaleate species (1304 and 1522 cm⁻¹) via sequential CB oxidation, ring-opening and dehydration are observed [41,42]. The band at 1556 cm⁻¹ can be attributed to carboxylate species (COO⁻), which is also one of the important oxidation intermediates [43]. The band at 1614 cm⁻¹ is attributed to the aromatic ring of adsorbed CB over the catalyst surface [8]. After 5 min, surface manganese carbonate species located at 1361 and 1371 cm⁻¹ appear [44]. With increasing the reaction time, a new peak at 1540 cm⁻¹ appears and strengthens gradually. That can be assigned to the species accumulation of aromatic ring adsorbed on the surface, suggesting the M-Cl or HCs-Cl depositions [43, 45]. On the contrary, a new peak between 1000 and 1200 cm⁻¹ appears on the P/MnCe, which is assigned to the alkoxide species [46,47]. The

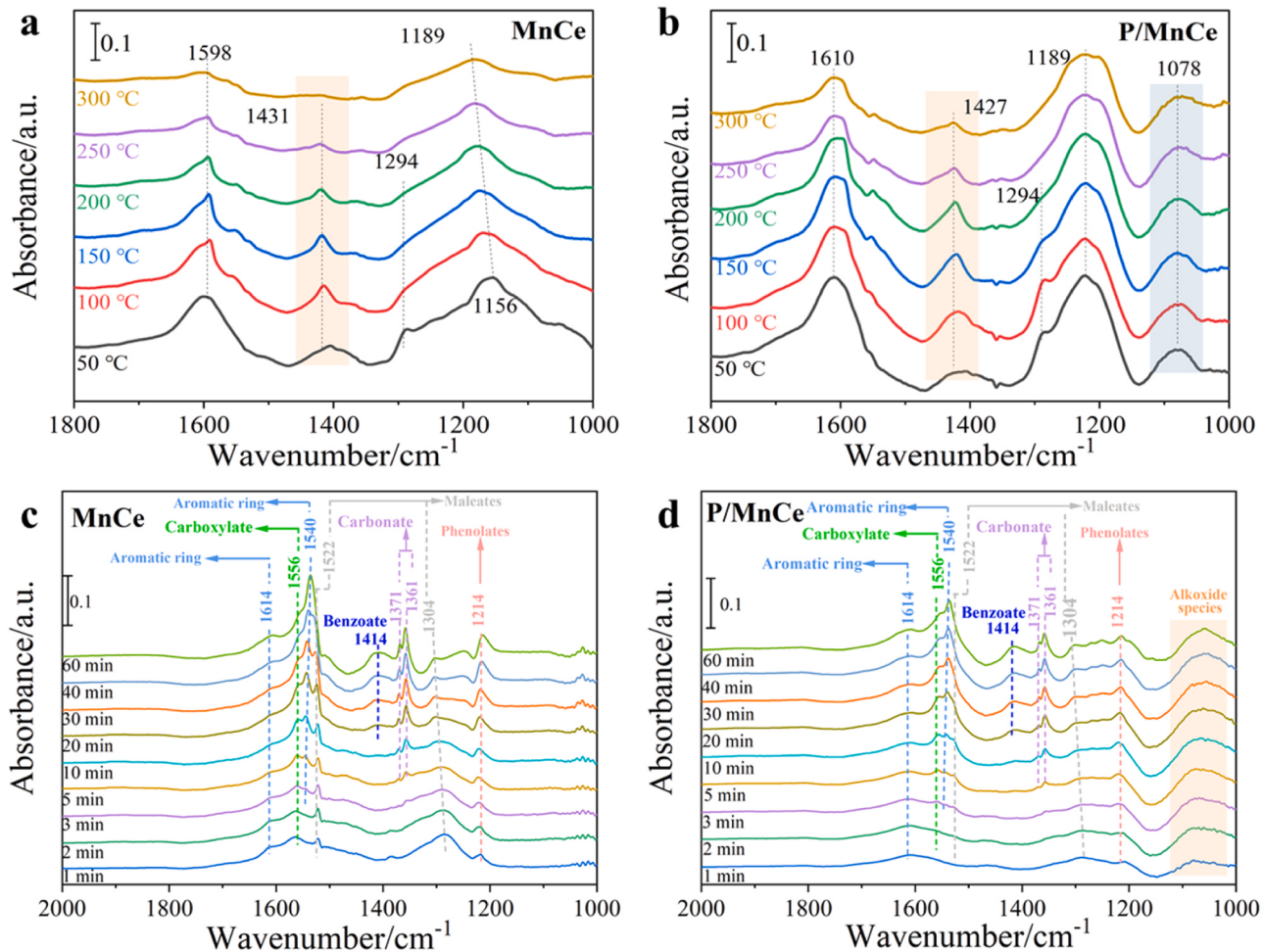


Fig. 4. In situ DRIFTS of NH_3 activation of (a) MnCe and (b) P/MnCe catalysts in 50–300 °C, and in situ DRIFTS of CB activation of (c) MnCe and (d) P/MnCe catalysts at 300 °C.

above results reveal that phosphate promotes the hydrolysis process of CB via surface hydroxyls. In addition, fewer intermediates and chlorine deposition are observed on the P/MnCe.

3.4. Chlorine products analysis

In order to obtain the composition of the deposited species on the used catalysts, TG-IR-MS tests are conducted (Fig. 5). The weight loss of the uMnCe and uP/MnCe are 2.40% and 3.03% in N_2 atmosphere up to 900 °C, respectively. With the assistance of IR peaks and MS signals, the weight loss could be divided into three stages: (1) weakly adsorbed reactants and products (CB or H_2O) desorbed from catalyst surface in 100–300 °C, (2) accumulated HCs and byproducts decomposed in 300–600 °C, and (3) deposited HCs-Cl and partial lattice oxygen above 600 °C. The H_2O release on the uP/MnCe occurs at lower temperature and larger amount than that on the uMnCe. It could be due to the combination of surface hydroxyl radicals, adsorbed H_2O and decomposition of phosphates [48], which is further confirmed by the TG-IR curves of MnCe and P/MnCe (Fig. S13). A small MS signal of CB is observed on the uMnCe at 180 °C. In contrast, no CB signal is observed on the uP/MnCe, indicating that almost all the inlet CB on the P/MnCe is converted to CO_2 or deposited intermediates in the MPC reactions. In addition, most of CO_2 releases above 200 °C, and two distinct bands centered at 300 and 600 °C could be observed on both the catalysts. They can be due to the decomposition of surface HCs rather than HCs-Cl. The MS signal of HCl is observed on the catalysts and the initial release of uP/MnCe is lower in temperature and quantity than that of uMnCe.

The results indicate that the amount of chlorine deposition on the catalyst is mitigated by the phosphate introduction. Moreover, no signals of Cl_2 or chlorine-containing species is detected during the temperature program. As known, the continuous releasing of H_2O and CO_2 above 600 °C are resulting from the decomposition of surface HCs and the releasing of HCl around 750 °C are resulting from the decomposition of M-Cl or HCs-Cl. Considering the relatively low formation temperature of HCl on the uP/MnCe, it is possible that the bonding strength of chlorine on Mn cations is weakened by the phosphate introduction.

It is generally believed that the dechlorination is the first step in CB oxidation because the bond energy of C-Cl (328 kJ/mol) is lower than that of C-H (414 kJ/mol). Then, chlorine dissociated from benzene ring is attracted and anchored on the surface cations. The effect of phosphate on chlorine adsorption energy (E_{ads}) is investigated by the DFT calculations. For the MnCeO₂ model, Cl inclines to form a new bond with surface oxygen ($E_{ads} = -3.49$ eV) (Fig. S14a). As for the MnCeO_v model, Cl occupies the position of oxygen vacancy accompanied by the formation of a novel Ce-Cl-Ce or Mn-Cl-Ce groups (Fig. 6a-b). The chlorine E_{ads} are -3.15 eV and -3.19 eV, respectively. The results indicate that chlorine could strongly anchor on both perfect and reduced surfaces. Moreover, the chlorine E_{ads} of P/MnCeO₂ (-2.44 eV vs. -3.49 eV) and P/MnCeO_v (-1.67 eV vs. -3.19 eV) significantly decrease compared to those of MnCeO₂ and MnCeO_v models (Figs. S14b and 6c), which could be due to the strongly electronic acceptors of chlorine from surface Mn-Cl-Ce. Combined with the Bader charge analysis of MnCeO_v and P/MnCeO_v models (Fig. S9), the enrichment of electrons at Mn and Ce cations could transfer to Cl ions, however, the charge density difference

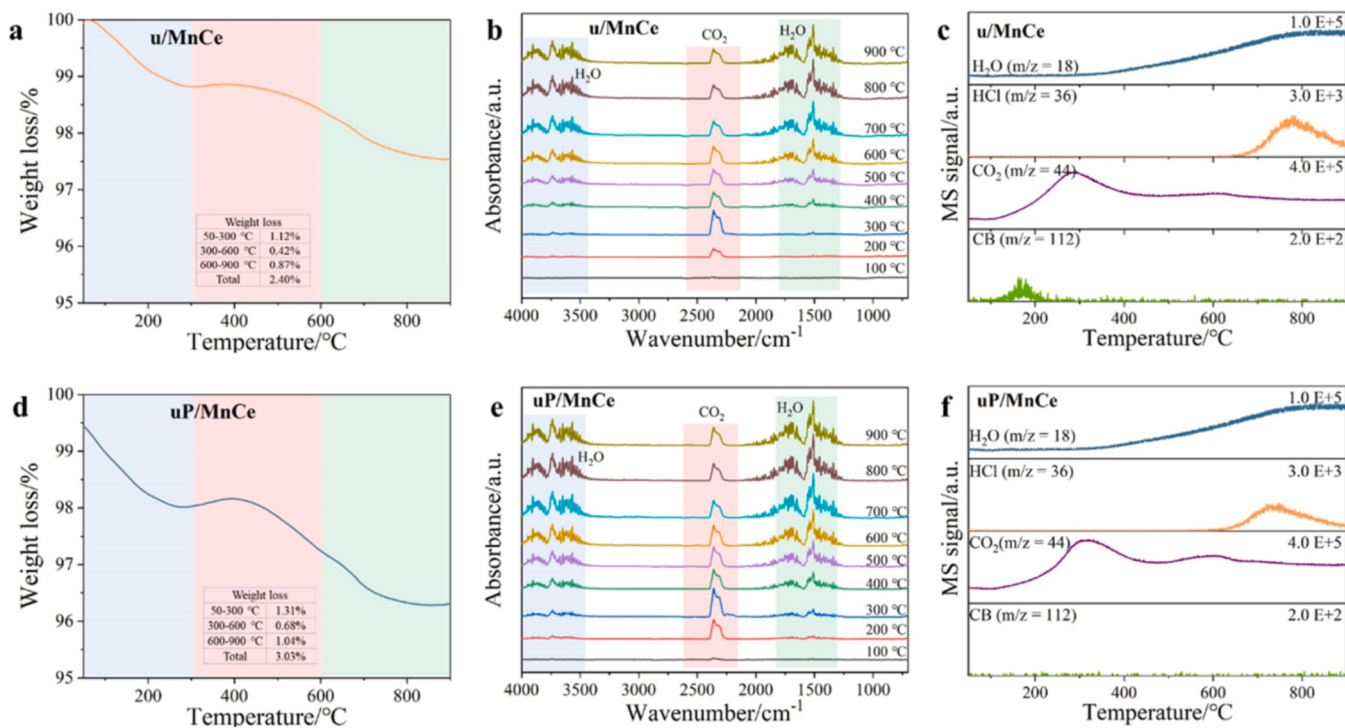


Fig. 5. TG-IR-MS results of u/MnCe and uP/MnCe catalysts. (a), (d) TG curves, (b), (e) IR spectra of the desorption gases, and (c), (f) MS signals.

and the Bader charge reveal that the charge of anchored-Cl decreases from 0.688 and 0.702–0.351 on the P/MnCeO_v due to the weakness of gain electron ability of chlorine. In other words, the electrons transfer from surface Mn or Ce cations to Cl ions could be suppressed by the phosphate introduction.

To further study the influence of phosphate on the orbital's population of chlorine, Total DOS of chlorine adsorption configurations is calculated. For the MnCeO_v model, the top of valance band is the mixtures of Cl, Mn and Ce without orbital polarization (The DOS of spin up and spin down is axial symmetry.), however, a clearly orbital polarization of Cl ions can be observed on the DOS of P/MnCeO_v models around ~ 14 eV and at the Fermi level, while the bottoms of Mn and Ce conduction band are nearly unchanged. The mixture extent of valence band between Mn or Ce and Cl decreases by the phosphate introduction, which show a good accordance with the differential charge density. The results indicate that the chlorine adsorption is significantly disturbed. The orbital polarization activates the adsorbed chlorine species on surface cations, lowering the binding strength of Cl with Mn or Ce and further promoting the dissociation of Cl ions from the surface.

Therefore, we search the transition states and calculate the energy barriers of the HCl formation reactions on the MnCeO_v and P/MnCeO_v models to confirm the results above (Fig. 6d–e). Anchored-Cl dissociates from O atom, and then binds with H of Ce-O(H)-Ce or P-OH to form HCl. The reaction energy barriers are 2.34 and 0.70 eV on the MnCeO_v and P/MnCeO_v models, respectively. The significant decrease of energy barrier indicates that HCl is facile to form and release from the P/MnCeO_v model. Thus, we propose that phosphate mitigates the electrons transfer from Ce or Mn to Cl, weakening the bonding orbitals mixture through the orbital polarization. This promotes the migration and transformation of Cl ions, thereby suppressing the deposition of polychlorinated species.

3.5. Dual-balance strategy

Previous work propose that the MnO₂-CeO₂ exhibits excellent MPC performance of NO_x and CB catalytic control because of its high reducibility of Mn for CB oxidation and low NH₃ unselective catalytic oxidation with O₂. However, compared to the HC deposition, the

surface chlorine accumulation has a greater impact on the activity of CB oxidation resulting from the stable bondage to oxygen vacancies and inhibiting of the O₂ adsorption and activation. Here we illustrate a dual-balance strategy on the phosphate-modified MnO₂-CeO₂ catalyst to improve the MPC performance. The understanding of the dual-balance mechanism is (Scheme 1): (1) The first level is the balance of reducibility and total acidity of the catalyst. Phosphate decreases the reducibility of the catalyst cations by stretching the bond length of Ce-O back to 2.42 Å and broadening the band gap of Mn 3d orbitals. Meanwhile, the number of oxygen vacancies is also promoted for facile H₂O adsorption and dissociation to form surface hydroxyls. Therefore, the total surface acidity also improved, which is mainly contributed by the Brønsted acid sites at high temperature. This balance mitigates the over-oxidation of NH₃ during SCR and enhances the nucleophilic substitutions of CB on Brønsted acid sites. (2) The second level is the number and strength balance of the Lewis and Brønsted acid sites of the catalyst. Phosphate increases both the Lewis and Brønsted acid sites in quantity even at 300 °C, however, the strength of Lewis acid sites binding to NH₃ and Cl is suppressed via the modulation of electronic structure on the Mn-Cl-Ce groups. Phosphate confines the electrons transferred from Ce or Mn cations to Cl ions, weakening the bonding orbitals mixture by the orbital polarization effect. This balance ensures enough acidity involved in the SCR reactions at high temperatures and lowers the energy barriers of Cl ions dissociation and HCl formation on the catalyst surface.

In addition to the catalytic performance, the recovery and regeneration of P/MnCe catalysts are also crucial for the industrial applications. Heat treatment and water washing can be employed as potential approaches to remove carbon deposition and chlorine accumulation on the deactivated surfaces of P/MnCe catalysts, respectively. Additionally, the issues of P leakage will be taken into consideration in future studies.

4. Conclusion

We elucidate a novel dual-balance strategy via phosphate modulation on the MnO₂-CeO₂ catalysts for the synergistic catalytic control of NO_x and CB. In addition to the increased NO_x and CB conversions above 150 °C, the N₂, CO₂, and HCl selectivitie can be also improved. The side

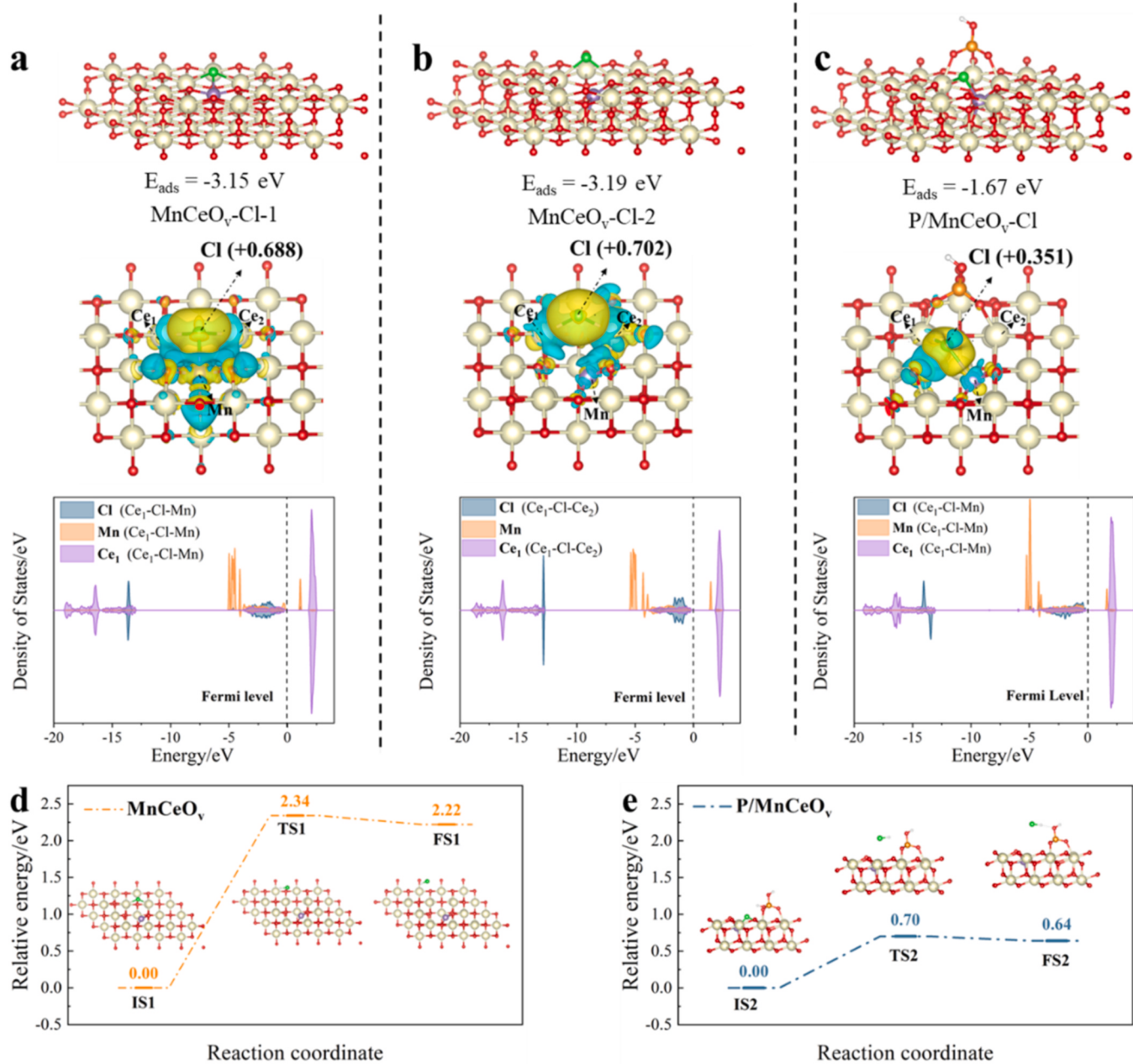


Fig. 6. Configurations of Cl adsorption with corresponding charge difference density, bader charge, and DOS of the (a) MnCeO_v-Cl-1, (b) MnCeO_v-Cl-2, and (c) P/MnCeO_v-Cl models. Relative energy profiles with corresponding structures of HCl formation on the (d) MnCeO_v, and P/MnCeO_v models. (For charge difference density, yellow and blue represent charge accumulation and depletion, respectively).

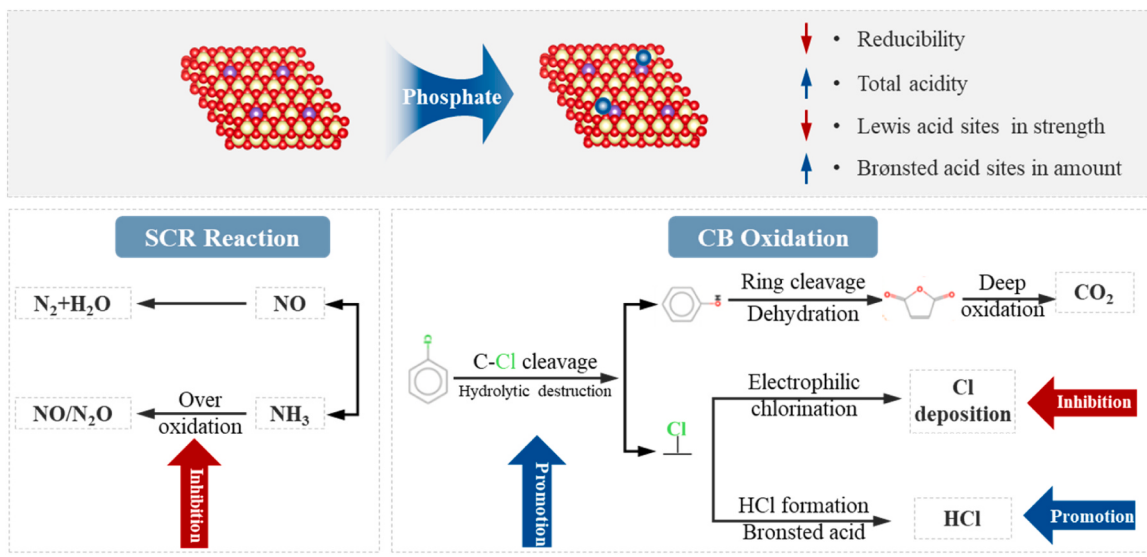
reactions of NH₃ unselective oxidation and chlorine deposition are also suppressed. We employed in situ spectroscopy and DFT calculation to identify the chemical descriptors on the catalytic performance. The bond length of Ce-O recovers from 2.18 Å in MnCe to 2.42 Å in P/MnCe, which is similar to that in CeO₂ 2.37 Å, mitigating the over-strong reducibility of Mn. NH₃ adsorption energy at Lewis acid sites and oxygen vacancy formation energy both decrease. In addition, phosphates can serve as novel Brønsted acid sites and decreased strength of Lewis acid sites. Phosphate mitigates the electrons transferred from Ce or Mn to Cl, weakening the bonding orbitals mixture by the orbital polarization and suppressing the deposition of polychlorinated species. This work provides a novel modulation strategy of dual-balance (reducibility vs. total acidity; Lewis vs. Brønsted acid sites in quantity and strength) on the environmental catalysts' design.

CRediT authorship contribution statement

Xiao Zhu: Conceptualization, Methodology, Investigation, Writing – original draft. **Xing Yuan:** Conceived the project, results discussion, reviewing and editing. **Zijian Song:** Results discussion and reviewing. **Yue Peng:** Writing – review & editing, Supervision. **Junhua Li:** Supervision. All authors have approved the final version of the manuscript.

Declaration of Competing Interest

The authors declare that they have no known competing financial interests or personal relationships that could have appeared to influence the work reported in this paper.



Scheme 1. Improvement mechanism of the phosphate-modified MnCe catalyst in the MPC reactions.

Data Availability

No data was used for the research described in the article.

Acknowledgments

This work was supported by the National Natural Science Foundation of China (22022605 and T2341002), National Key Research and Development Program of China (2022YFC3702004). We are grateful for the technical support from the Center of High performance computing, Tsinghua University.

Appendix A. Supporting information

Supplementary data associated with this article can be found in the online version at [doi:10.1016/j.apcatb.2023.123364](https://doi.org/10.1016/j.apcatb.2023.123364).

References

- [1] M. Zhu, J.K. Lai, U. Tumuluri, Z. Wu, I.E. Wachs, Nature of active sites and surface intermediates during SCR of NO with NH₃ by supported V₂O₅-WO₃/TiO₂ catalysts, *J. Am. Chem. Soc.* 139 (2017) 15624–15627.
- [2] Z. Lian, L. Liu, C. Lin, W. Shan, H. He, Hydrothermal aging treatment activates V₂O₅/TiO₂ catalysts for NO_x abatement, *Environ. Sci. Technol.* 56 (2022) 9744–9750.
- [3] W. Hu, T. Selleri, F. Gramigni, E. Fenes, K.R. Rout, S. Liu, I. Nova, D. Chen, X. Gao, E. Tronconi, On the redox mechanism of low-temperature NH₃-SCR over Cu-CHA: a combined experimental and theoretical study of the reduction half cycle, *Angew. Chem. Int. Ed.* 60 (2021) 7197–7204.
- [4] Y. Zhang, Y. Peng, K. Li, S. Liu, J. Chen, J. Li, F. Gao, C.H.F. Peden, Using transient FTIR spectroscopy to probe active sites and reaction intermediates for selective catalytic reduction of NO on Cu/SSZ-13 catalysts, *ACS Catal.* 9 (2019) 6137–6145.
- [5] Y. Long, Y. Su, Y. Xue, Z. Wu, X. Weng, V₂O₅-WO₃/TiO₂ catalyst for efficient synergistic control of NO_x and chlorinated organics: insights into the arsenic effect, *Environ. Sci. Technol.* 55 (2021) 9317–9325.
- [6] X. Yuan, Y. Peng, X. Zhu, H. Wang, Z. Song, W. Si, Y. Wang, J. Li, Anti-poisoning mechanisms of Sb on vanadia-based catalysts for NO_x and chlorobenzene multi-pollutant control, *Environ. Sci. Technol.* 57 (2023) 10211–10220.
- [7] Y. Su, K. Fu, C. Pang, Y. Zheng, C. Song, N. Ji, D. Ma, X. Lu, C. Liu, R. Han, Q. Liu, Recent advances of chlorinated volatile organic compounds' oxidation catalyzed by multiple catalysts: reasonable adjustment of acidity and redox properties, *Environ. Sci. Technol.* 56 (2022) 9854–9871.
- [8] Z. Song, Y. Peng, X. Zhao, H. Liu, C. Gao, W. Si, J. Li, Roles of Ru on the V₂O₅-WO₃/TiO₂ catalyst for the simultaneous purification of NO_x and chlorobenzene: a dechlorination promoter and a redox inductor, *ACS Catal.* 12 (2022) 11505–11517.
- [9] G. Li, K. Shen, L. Wang, Y. Zhang, H. Yang, P. Wu, B. Wang, S. Zhang, Synergistic degradation mechanism of chlorobenzene and NO over the multi-active center catalyst: the role of NO₂, Brønsted acidic site, oxygen vacancy, *Appl. Catal. B* 286 (2021), 119865.
- [10] G. Li, L. Wang, P. Wu, S. Zhang, K. Shen, Y. Zhang, Insight into the combined catalytic removal properties of Pd modification V/TiO₂ catalysts for the nitrogen oxides and benzene by: an experiment and DFT study, *Appl. Surf. Sci.* 527 (2020), 146787.
- [11] L. Gan, W. Shi, K. Li, J. Chen, Y. Peng, J. Li, Synergistic promotion effect between NO_x and chlorobenzene removal on MnO_x-CeO₂ catalyst, *ACS Appl. Mater. Interfaces* 10 (2018) 30426–30432.
- [12] L. Gan, Y. Wang, J. Chen, T. Yan, J. Li, J. Crittenden, Y. Peng, The synergistic mechanism of NO_x and chlorobenzene degradation in municipal solid waste incinerators, *Catal. Sci. Technol.* 9 (2019) 4286–4292.
- [13] C. Zhang, J. Zhang, Y. Shen, J. He, W. Qu, J. Deng, L. Han, A. Chen, D. Zhang, Synergistic catalytic elimination of NO_x and chlorinated organics: cooperation of acid sites, *Environ. Sci. Technol.* 56 (2022) 3719–3728.
- [14] J. Chen, L. Guo, H. Zhu, Y. Qiu, D. Yin, T. Zhang, J. Chen, Y. Peng, J. Li, Balancing redox and acidic properties for optimizing catalytic performance of SCR catalysts: a case study of nanopolyhedron CeO_x-supported WO₃, *J. Environ. Chem. Eng.* 9 (2021), 105828.
- [15] F. Lin, Z. Zhang, N. Li, B. Yan, C. He, Z. Hao, G. Chen, How to achieve complete elimination of Cl-VOCs: a critical review on byproducts formation and inhibition strategies during catalytic oxidation, *Chem. Eng. J.* 404 (2021), 126534.
- [16] Y. Guo, M. Wen, G. Li, T. An, Recent advances in VOC elimination by catalytic oxidation technology onto various nanoparticles catalysts: a critical review, *Appl. Catal. B* 281 (2021), 119447.
- [17] C. He, J. Cheng, X. Zhang, M. Douthwaite, S. Patisson, Z. Hao, Recent advances in the catalytic oxidation of volatile organic compounds: a review based on pollutant sorts and sources, *Chem. Rev.* 119 (2019) 4471–4568.
- [18] F. Castellino, S.B. Rasmussen, A.D. Jensen, J.E. Johnsson, R. Fehrmann, Deactivation of vanadia-based commercial SCR catalysts by polyphosphoric acids, *Appl. Catal. B* 83 (2008) 110–122.
- [19] P. Wang, S. Gao, H. Wang, S. Chen, X. Chen, Z. Wu, Enhanced dual resistance to alkali metal and phosphate poisoning: Mo modifying vanadium-titanate nanotubes SCR catalyst, *Appl. Catal. A* 561 (2018) 68–77.
- [20] T. Yi, Y. Zhang, J. Li, X. Yang, Promotional effect of H₃PO₄ on ceria catalyst for selective catalytic reduction of NO by NH₃, *Chin. J. Catal.* 37 (2016) 300–307.
- [21] Q. Dai, Z. Zhang, J. Yan, J. Wu, G. Johnson, W. Sun, X. Wang, S. Zhang, W. Zhan, Phosphate-functionalized CeO₂ nanosheets for efficient catalytic oxidation of dichloromethane, *Environ. Sci. Technol.* 52 (2018) 13430–13437.
- [22] X. Dai, X. Wang, Y. Long, S. Patisson, Y. Lu, D.J. Morgan, S.H. Taylor, J.H. Carter, G.J. Hutchings, Z. Wu, X. Weng, Efficient elimination of chlorinated organics on a phosphoric acid modified CeO₂ catalyst: a hydrolytic destruction route, *Environ. Sci. Technol.* 53 (2019) 12697–12705.
- [23] Y. Long, J. Liu, M. Chen, R. Li, X. Weng, Z. Wu, Catalytic destruction of chlorobenzene over K-OMS-2: inhibition of high toxic byproducts via phosphate modification, *J. Environ. Sci.* 127 (2023) 844–854.
- [24] J. Hafner, Ab-initio simulations of materials using VASP: Density-functional theory and beyond., 29 (2008) 2044–2078.
- [25] W. Song, J. Liu, H. Zheng, S. Ma, Y. Wei, A. Duan, G. Jiang, Z. Zhao, E.J.M. Hensen, A mechanistic DFT study of low temperature SCR of NO with NH₃ on MnCe_{1-x}O₂(111), *Catal. Sci. Technol.* 6 (2016) 2120–2128.
- [26] Z. Song, S. Yu, H. Liu, Y. Wang, C. Gao, Z. Wang, Y. Qin, Y. Peng, J. Li, Carbon/chlorinate deposition on MnO_x-CeO₂ catalyst in chlorobenzene combustion: the effect of SCR flue gas, *Chem. Eng. J.* 433 (2022), 133552.
- [27] S. Xiong, Y. Liao, X. Xiao, H. Dang, S. Yang, Novel effect of H₂O on the low temperature selective catalytic reduction of NO with NH₃ over MnO_x-CeO₂: mechanism and kinetic study, *J. Phys. Chem. C.* 119 (2015) 4180–4187.

[28] X. Yao, K. Ma, W. Zou, S. He, J. An, F. Yang, L. Dong, Influence of preparation methods on the physicochemical properties and catalytic performance of $\text{MnO}_x\text{-CeO}_2$ catalysts for $\text{NH}_3\text{-SCR}$ at low temperature, *Chin. J. Catal.* 38 (2017) 146–159.

[29] W. Jiang, Y. Yu, F. Bi, P. Sun, X. Weng, Z. Wu, Synergistic elimination of NO_x and chloroaromatics on a commercial $\text{V}_2\text{O}_5\text{-WO}_3\text{/TiO}_2$ catalyst: byproduct analyses and the SO_2 effect, *Environ. Sci. Technol.* 53 (2019) 12657–12667.

[30] W. Xingyi, K. Qian, L. Dao, Catalytic combustion of chlorobenzene over $\text{MnO}_x\text{-CeO}_2$ mixed oxide catalysts, *Appl. Catal., B* 86 (2009) 166–175.

[31] J. Quiroz, J.-M. Giraudon, A. Gervasini, C. Dujardin, C. Lancelot, M. Trentesaux, J.-F. Lamonier, Total oxidation of formaldehyde over $\text{MnO}_x\text{-CeO}_2$ catalysts: the effect of acid treatment, *ACS Catal.* 5 (2015) 2260–2269.

[32] J. Zhang, D. Tan, Q. Meng, X. Weng, Z. Wu, Structural modification of LaCoO_3 perovskite for oxidation reactions: The synergistic effect of Ca^{2+} and Mg^{2+} co-substitution on phase formation and catalytic performance, *Appl. Catal., B* 172–173 (2015) 18–26.

[33] M. Li, M. Gao, G. He, Y. Yu, H. He, Mechanistic insight into the promotion of the low-temperature NH_3 -selective catalytic reduction activity over $\text{Mn}_x\text{Ce}_{1-x}\text{O}_y$ catalysts: a combined experimental and density functional theory study, *Environ. Sci. Technol.* 57 (2023) 3875–3882.

[34] F. Yang, J. Graciani, J. Evans, P. Liu, J. Hrbek, J.F. Sanz, J.A. Rodriguez, CO oxidation on inverse $\text{CeO}_x\text{/Cu}(111)$ catalysts: high catalytic activity and ceria-promoted dissociation of O_2 , *J. Am. Chem. Soc.* 133 (2011) 3444–3451.

[35] H. Zhao, H. Li, Z. Pan, F. Feng, Y. Gu, J. Du, Y. Zhao, Design of CeMnCu ternary mixed oxides as soot combustion catalysts based on optimized Ce/Mn and Mn/Cu ratios in binary mixed oxides, *Appl. Catal., B* 268 (2020), 118422.

[36] R. Liu, Y. Xu, F. Ye, F. Jia, R. Xu, Influence of transition metal (Fe, Co, and Ag) doping on the $\text{MnO}_x\text{-CeO}_2\text{/Ti}$ -bearing blast furnace slag catalyst for selective catalytic reduction of NO_x with NH_3 at low temperature, *N. J. Chem.* 41 (2017) 11299–11307.

[37] F. Gao, X. Tang, H. Yi, J. Li, S. Zhao, J. Wang, C. Chu, C. Li, Promotional mechanisms of activity and SO_2 tolerance of Co- or Ni-doped $\text{MnO}_x\text{-CeO}_2$ catalysts for SCR of NO_x with NH_3 at low temperature, *Chem. Eng. J.* 317 (2017) 20–31.

[38] G. Qi, R.T. Yang, Characterization and FTIR studies of $\text{MnO}_x\text{-CeO}_2$ catalyst for low-temperature selective catalytic reduction of NO with NH_3 , *J. Phys. Chem. B* 108 (2004) 15738–15747.

[39] J. Mu, X. Li, W. Sun, S. Fan, X. Wang, L. Wang, M. Qin, G. Gan, Z. Yin, D. Zhang, Inductive effect boosting catalytic performance of advanced $\text{Fe}_{1-x}\text{V}_x\text{O}_8$ catalysts in low-temperature NH_3 selective catalytic reduction: insight into the structure, interaction, and mechanisms, *ACS Catal.* 8 (2018) 6760–6774.

[40] S. Lommicki, J. Lichtenberger, Z. Xu, M. Waters, J. Kosman, M.D. Amiridis, Catalytic oxidation of 2,4,6-trichlorophenol over vanadia/titania-based catalysts, *Appl. Catal., B* 46 (2003) 105–119.

[41] J. Lichtenberger, Catalytic oxidation of chlorinated benzenes over $\text{V}_2\text{O}_5\text{/TiO}_2$ catalysts, *J. Catal.* 223 (2004) 296–308.

[42] J. Wang, X. Wang, X. Liu, J. Zeng, Y. Guo, T. Zhu, Kinetics and mechanism study on catalytic oxidation of chlorobenzene over $\text{V}_2\text{O}_5\text{/TiO}_2$ catalysts, *J. Mol. Catal. A: Chem.* 402 (2015) 1–9.

[43] P. Sun, W. Wang, X. Dai, X. Weng, Z. Wu, Mechanism study on catalytic oxidation of chlorobenzene over $\text{Mn}_x\text{Ce}_{1-x}\text{O}_2\text{/H-ZSM5}$ catalysts under dry and humid conditions, *Appl. Catal. B* 198 (2016) 389–397.

[44] L. Ye, P. Lu, Y. Peng, J. Li, H. Huang, Impact of NO_x and NH_3 addition on toluene oxidation over $\text{MnO}_x\text{-CeO}_2$ catalyst, *J. Hazard. Mater.* 416 (2021), 125939.

[45] H. Sun, Z. Liu, S. Chen, X. Quan, The role of lattice oxygen on the activity and selectivity of the OMS-2 catalyst for the total oxidation of toluene, *Chem. Eng. J.* 270 (2015) 58–65.

[46] W. Yang, Z. Su, Z. Xu, W. Yang, Y. Peng, J. Li, Comparative study of α -, β -, γ - and δ - MnO_2 on toluene oxidation: oxygen vacancies and reaction intermediates, *Appl. Catal. B* 260 (2020), 118150.

[47] S. Mo, Q. Zhang, J. Li, Y. Sun, Q. Ren, S. Zou, Q. Zhang, J. Lu, M. Fu, D. Mo, J. Wu, H. Huang, D. Ye, Highly efficient mesoporous MnO_2 catalysts for the total toluene oxidation: oxygen-vacancy defect engineering and involved intermediates using in situ DRIFTS, *Appl. Catal., B* 264 (2020), 118464.

[48] X. Guo, Q. Fan, L. Yu, J. Liang, W. Ji, L. Peng, X. Guo, W. Ding, Y. Chen, Sandwich-like LiFePO_4 /graphene hybrid nanosheets: in situ catalytic graphitization and their high-rate performance for lithium ion batteries, *J. Mater. Chem. A* 1 (2013) 11534.